Supplementary Information

Robust Iron-based Fischer-Tropsch Catalysts by Direct Joule Synthesis

Jose Recatala-Gomez,‡[a,b] Somya Verma,‡[a,c,d] Puneethkumar M. Srinivasappa,[a,c] Mona Abdelgaid,[b,f,g] Tangsheng Zou,[c] Seohyeong Lee,[d] Delwin Tanto,[d] Pei Ying Moo,[c] Chun Qi Joy Ng,[c] Chuandayani Gunawan Gwie,[c] Chenguang Zhang,[d] Zainul Aabdin,[e] Kristin A. Persson,[b,f,g] Kedar Hippalgaonkar,[a,d] Amol Amrute*[c]*

[a] Berkeley Education Alliance for Research in Singapore (BEARS), 1 Create Way, #05-02/03, CREATE Tower, 138602 Singapore.

[b] Department of Materials Science & Engineering, University of California, Berkeley, California 94720, United States

[c] Institute of Sustainability for Chemicals, Energy and Environment ($ISCE^2$), Agency for Science, Technology and Research (A*STAR), 1 Pesek Road, Jurong Island, 627833, Singapore

[d] School of Materials Science and Engineering, Nanyang Technological University, 50 Nanyang Avenue, 639798 Singapore

[e] Institute of Materials Research and Engineering (IMRE), Agency for Science, Technology and Research (A*STAR), 2 Fusionopolis Way, #08-03 Innovis, Singapore 138634

[f] Bakar Institute of Digital Materials for the Planet, University of California at Berkeley, Berkeley, California 94720, United States

[g] Materials Science Division, Lawrence Berkeley National Laboratory, Berkeley, California 94720, United States

*Correspondence authors: ***kedar@ntu.edu.sg***, ***amol_amrute@a-star.edu.sg***

Supporting Information Details:

Number of Pages: 29

Number of Figures: 10

Number of Tables: 4

Contents:

S1. Experimental methods
S1.1 Catalyst characterisation techniques
S1.2 Catalyst testing and product quantification
S1.3 Computational model construction and validation
S2. Catalyst characterisation, pretreatment and performance comparison
S2.1 Surface morphology and structural properties of FeCoNa catalysts
S2.2 Role of catalyst pretreatment on CO_2 hydrogenation over DJS-derived catalysts
S2.3 Comparison of catalytic performance and stability with literature catalysts
S3. N_2-sorption
S4. SEM, XPS and surface characterisation
S5. Long-term stability and thermal behaviour of DJS-made FeCoNa catalyst during CO_2 hydrogenation
S6. Computational analysis
S7. Supplementary references

S1. Experimental methods

S1.1 Catalyst characterisation techniques

X-ray diffraction (XRD) measurements were performed using a Rigaku SmartLab 3 kW diffractometer operated in coupled θ-2θ geometry with Cu Kα radiation (λ = 1.5406 Å) at 40 kV and 40 mA. Diffraction patterns were recorded over a 2θ range of 20-80° and at a scan rate of 2° min^{-1} with a step size of 0.02°. Phase identification was carried out by comparison with reference patterns from the Inorganic Crystal Structure Database (ICSD). Rietveld refinement and quantitative phase analysis were performed using TOPAS software.

N_2 adsorption-desorption measurements were conducted at −196.15 °C using a Micromeritics ASAP 2420MP static volumetric adsorption analyser. Before analysis, the samples were degassed under vacuum at 200 °C for 24 h to remove physically adsorbed species. Specific surface areas were calculated using the Brunauer-Emmett-Teller method. Total pore volumes were estimated from the adsorption branch near saturation pressure, while pore-size distributions and average pore diameters were derived using the Barrett-Joyner-Halenda method.

Scanning electron microscopy (SEM) was performed using a JEOL JSM-7800F field-emission scanning electron microscope equipped with an Oxford Instruments energy-dispersive X-ray (EDX) spectroscopy detector. Dry powder samples were directly mounted onto conductive carbon tape on an SEM sample stub without prior dispersion. Images and elemental analyses were acquired at an accelerating voltage of 20 kV.

For Transmission Electron Microscopy (TEM) analysis, the catalyst powder was dispersed in ethanol at a concentration of approximately 1 mg mL^{-1} and sonicated for 10 min. A 10 μL aliquot of the suspension was drop-cast onto a carbon-coated copper grid with 200 mesh and dried under

ambient conditions before analysis. High-resolution transmission electron microscopy (HR-TEM) was performed using a Titan 80-300 kV microscope equipped with a 4096 × 4096 pixel OneView CMOS camera. Images were acquired from multiple regions at magnifications ranging from 3,800× to 490,000× using the full camera resolution and an exposure time of 1 s. Selected-area electron diffraction patterns were collected from several regions using a selected-area aperture of 580 nm. An aperture of approximately 150 nm was used for diffraction measurements from individual grains. For all diffraction measurements, the camera length was fixed at 1.1 m, and the exposure time was 2 s.

Scanning transmission electron microscopy imaging and EDX elemental mapping were carried out using a Talos 80-200 kV microscope equipped with a 4096 × 4096-pixel Ceta camera and Super-X four silicon drift detectors. The microscope was operated at an accelerating voltage of 200 kV.

X-ray photoelectron spectroscopy (XPS) measurements were carried out using a Kratos AXIS Supra spectrometer equipped with a hemispherical analyser and a monochromatic Al Kα X-ray source with a photon energy of 1486.6 eV, operated at 15 kV and 15 mA. Spectra were collected over an analysis area of 700 × 300 μm^2 at a take-off angle of 90°. Pass energies of 160 and 20 eV were used for survey and high-resolution spectra, respectively. Charge neutralisation was achieved using a low-energy electron flood gun. Spectral deconvolution and peak fitting were performed using CasaXPS software.

Thermogravimetric analysis (TGA) was performed using a TA Instruments SDT 650 simultaneous thermal analyser with TRIOS software. Catalysts were analysed in separate runs under flowing air and N_2. Samples were heated from room temperature to 900 °C at 10 °C min^{-1} under a gas flow of

20 mL min^{-1} and then cooled to room temperature. The air and N_2 weight profiles were compared at the same temperature.

S1.2 Catalyst testing and product quantification

CO_2 hydrogenation reactions were evaluated using a 16-channel continuous-flow fixed-bed high-throughput reactor system developed by hte GmbH. Uniform gas flow distribution to each reactor was achieved using feed capillaries with identical dimensions (inner diameter = 100 μm, length = 2 m), while pressure regulation was controlled through downstream restriction capillaries (0.13 mm × 2 m). The entire setup was automated using hteControl software, with reactor operation, temperature programming, gas switching, and data acquisition managed *via* a programmable logic controller. Each reaction channel consisted of an Incoloy 800H tubular reactor with an inner diameter of 7.9 mm positioned inside a multi-zone furnace. For each catalytic test, 0.5 g of sieved catalyst (0.25-0.40 mm) was diluted with SiC to a total bed volume of 3 mL and loaded at the centre of the isothermal zone. The catalyst bed was sandwiched between SiC layers to improve heat transfer and minimise channelling. All reactors were leak-tested at pressures above the intended operating conditions. Before CO_2 hydrogenation, the catalysts were reduced at 400 °C for 20 h under pure H_2 flow (8 L h^{-1} for eight reactors) and subsequently activated at 300 °C and 10 bar for 24 h using a 2:1 H_2/CO mixture containing 33.33 vol.% CO and 66.67 vol.% H_2. The rationale for this reduction-activation procedure and its influence on catalyst performance is discussed in Supplementary Discussion S2.2. CO_2 hydrogenation was then carried out at 350 °C and 30 bar using a 3:1 H_2/CO_2 feed containing 22 vol.% CO_2, 66 vol.% H_2, and 12 vol.% Ar. Ar was used as an internal standard, and the gas hourly space velocity was maintained at 5732 cm^3 h^{-1} g_{cat}^{-1}. CO_2 conversion, product selectivities, and hydrocarbon yields were calculated from inlet and outlet molar flow rates determined by online gas chromatography.

Reaction effluents were analysed online using an Agilent Technologies 8890 gas chromatograph (GC) equipped with two flame ionisation detectors (FID) and two thermal conductivity detectors (TCD), connected to seven columns. The column configuration included FID-1 with Rtx-5 (5 m × 320 μm × 1 μm) and Rt-Q-BOND (30 m × 320 μm × 10 μm), FID-2 with hte01 (20 m × 180 μm × 1 μm), and both TCD-1 and TCD-2 with Rt-Q-BOND (5 m × 320 μm × 10 μm) and Rt-Msieve 5 Å (30 m × 320 μm × 30 μm). Gas sampling was performed using a 32-port VICI valve, enabling sequential injections from multiple reactor channels. To prevent condensation of all products, all transfer lines and heated zones were maintained at elevated temperatures: the 32-port VICI valve at 170 °C, the GC interface at 200 °C, and the condensers at 100 °C. CO_2 conversion and obtained product selectivities were calculated based on inlet and outlet molar flow rates using standard equations (provided below).

$$X(\mathrm{CO_2})\ (\%) = \frac{\mathrm{CO_{2,in}} - \mathrm{CO_{2,out}}}{\mathrm{CO_{2,in}}} \times 100 \qquad \text{..... (1)}$$

$$S(\mathrm{CO})\ (\%) = \frac{CO_{Out}}{\mathrm{CO_{2,in}} - \mathrm{CO_{2,out}}} \times 100 \qquad \text{..... (2)}$$

$$S(\mathrm{CH_4})\ (\%) = \frac{\mathrm{CH_{4,out}}}{\mathrm{CO_{2,in}} - \mathrm{CO_{2,out}}} \times 100 \qquad \text{..... (3)}$$

$$S(\mathrm{C_2 - C_4})\ (\%) = \frac{\mathrm{C_{2,out}} + \mathrm{C_{3,out}} + \mathrm{C_{4,out}}}{\mathrm{CO_{2,in}} - \mathrm{CO_{2,out}}} \times 100 \qquad \text{..... (4)}$$

$$S(C_{5+})\ (\%) = 100 - [S(\mathrm{CO}) + S(\mathrm{CH_4}) + S(\mathrm{C_2 - C_4}) + S(\mathrm{R - OH})] \qquad \text{..... (5)}$$

where the subscripts 'in' and 'out' represent the inlet and outlet molar flow rates of the corresponding component *i*.

The yield (Y_i) for each product was calculated as the product of its selectivity and CO_2 conversion according to the following relation:

$$Y_i\ (\%) = \frac{X(\mathrm{CO_2}) \times S_i}{100} \qquad \text{..... (6)}$$

The C_{2+} and C_{5+} space-time yield (*STY*) is calculated directly from CO_2 conversion, the corresponding product selectivity, and the gas hourly space velocity:

$$STY_i = \frac{X(CO_2)}{100} \times \frac{S_i}{100} \times \frac{GHSV}{10^6} \times \frac{10^5}{8.314 \times 273.15} \times \frac{1}{1 + r_{\mathrm{H_2/CO_2}}} \times 13.1 \qquad \text{..... (7)}$$

Where, i = C_{2+} or C_{5+}; STY_i is in $g_i\, h^{-1} g_{cat}^{-1}$, $X(CO_2)$ is CO_2 conversion (%) and S_i is the corresponding product selectivity (%), GHSV is in $cm^3\ h^{-1}\ g_{cat}^{-1}$, and $r_{\mathrm{H_2/CO_2}}$ is the H_2/CO_2 molar feed ratio (3 for the reported runs).

S1.3 Computational model construction and validation

The bulk χ-Fe_5C_2 (Hägg carbide) was optimised using a 2 × 5 × 4 Monkhorst-Pack k-point mesh. The three inequivalent Fe atoms exhibit magnetic moments of 2.140, 1.735, and 1.171 μB, while the C atom carries an opposite moment of −0.098 μB, yielding an average magnetic moment of 1.78 μB per Fe atom within the unit cell, in good agreement with previous experimental and theoretical values.[1–3] The computed lattice parameters (11.58 Å × 4.51 Å × 5.00 Å, β = 97.65°, α = γ = 90°) likewise agree well with the experimental values for Hägg carbide (a = 11.58 Å, b =

4.57 Å, c = 5.05 Å, β = 97.75°).[1,3–5] Furthermore, the bulk Fe_3O_4 was modelled using the conventional unit cell comprising 56 atoms ($Fe_{24}O_{32}$), sampled with a 4 × 4 × 4 k-point mesh. The optimised lattice parameters (a = b = c = 8.53 Å, α = β = γ = 90°) are in good agreement with the experimental values (a = b = c = 8.39 Å, α = β = γ = 90°).[6,7] To correctly capture the localised behaviour of the Fe 3d orbitals and account for the strong on-site Coulomb correlations, we employed an effective Hubbard parameter of 5.3 eV for iron.[8,9] Finally, FeCo was modelled as an ordered body-centred cubic structure with a CsCl-type B2 superlattice, in which the Fe and Co atoms occupy the corner and body-centre positions of the cubic cell, giving a stoichiometric 1:1 composition. A dense 8 × 8 × 8 Monkhorst-Pack k-point mesh was used to sample the Brillouin zone of this two-atom cell. The optimised lattice parameters (a = b = c = 2.84 Å, α = β = γ = 90°) agree well with the experimental B2 FeCo lattice constant (a = 2.85 Å). The calculated magnetic moment for the Fe atom was 2.772 μB and 1.735 μB for the Co atom, in good agreement with previous theoretical results.[10–12]

The surface models were constructed from the optimised bulk structures, with the specific facets chosen to reflect the crystallographic planes identified experimentally by FFT analysis of the fresh and spent catalyst samples. Specifically, we constructed the FeCo (110), Fe_3O_4 (111), and χ-Fe_5C_2 (510) surfaces. To probe the role of the sodium promoter, χ-Fe_5C_2 was modelled in its pristine form and with a Na_2O cluster deposited on the surface. Each slab was separated from its periodic replica by a vacuum layer of thickness of 15 Å to eliminate spurious interactions along the surface normal. The Brillouin-zone integrations were performed using a 3 × 3 × 1 Monkhorst-Pack k-point mesh. The bottom layers were fixed at their bulk-optimised positions to mimic the underlying bulk, while the top layers as well as the Na_2O cluster were allowed to relax during geometry optimisation. Zero-point energy and entropy corrections to the free energies were applied at the CO_2

hydrogenation temperature. The adsorption energy of the adsorbates (G_{ads}) is defined by $G_{ads} = G_{slab\ with\ adsorbate} - G_{slab} - G_{adsorbate}$, in which $G_{slab\ with\ adsorbate}$ represents the free energy of the adsorbed species together with the Fe-based catalyst model, G_{slab} is the free energy of the slab, and $G_{adsorbate}$ is the free energy of the species in the gas phase. In this definition, a more negative value indicates a stronger binding of the adsorbate to the catalyst.

S2. Catalyst characterisation, pretreatment and performance comparison

S2.1 Surface morphology and structural properties of FeCoNa catalysts

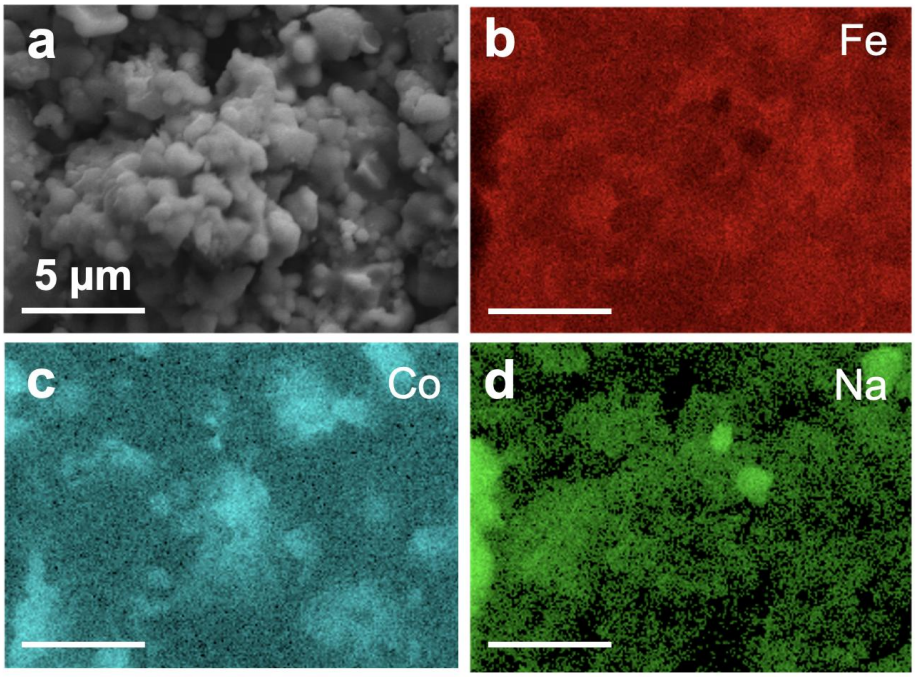


Fig. S1. Morphology and elemental distribution of the FeCoNa catalyst. (a) SEM image and corresponding EDX elemental maps of the DJS-derived FeCoNa catalyst, showing micron-scale particles and a broadly homogeneous distribution of (b) Fe, (c) Co, and (d) Na.

Table S1. Structural and surface properties of fresh and spent FeCoNa catalysts

Entry	Catalyst	State	S_{BET} (m^2/g)	V_{pore} (cm^3/g)	Crystallite Size, *d* (nm)			Phase Fraction (wt.%)[1]		
					FeCo	Fe_3O_4	Fe_5C_2	FeCo	Fe_3O_4	Fe_5C_2
1	FeCoNa	Fresh	1.2	0.01	55.4	-	-	77.4	-	22.6
2	FeCoNa-B25-4	Fresh	1.3	0.004	43.2	-	3.0	88.9	-	11.1
		Spent	5.1	0.015	46.4	145.0	35.9	6.4	64	29.6
3	FeCoNa-B25-4-Ar	Fresh	0.7	0.003	33.4	-	7.0	72.8	-	27.2
		Spent	5.2	0.015	42.1	80.3	45.0	6.1	41.9	52.0

[1] Phase fraction extracted by using Rietveld refinement.

S2.2 Role of catalyst pretreatment on CO_2 hydrogenation over DJS-derived catalysts

In the CO_2 hydrogenation reaction, the pretreatment step (reduction and activation) is considered crucial for achieving high catalytic performance over Fe-based catalysts due to the formation of active oxide-carbide phases.[13–15] To identify the most effective pretreatment sequence and elucidate its structural influence on DJS-derived catalysts, the CO_2 hydrogenation reaction was evaluated over the FeCoNa-B25-4 catalyst under both non-pretreated and pretreated conditions at 350 °C, 30 bar, and a GHSV of 5732 $cm^3\ h^{-1}\ g_{cat}^{-1}$ for 40 h on stream (**Fig. S2**). In the absence of pretreatment, the FeCoNa-B25-4 catalyst achieved a CO_2 conversion of 47% with a C_{5+} selectivity of ~17%. In contrast, the introduction of a pretreatment step significantly enhanced catalytic performance, increasing CO_2 conversion to ~57% and C_{5+} selectivity to ~34%. These results clearly demonstrate that the FeCoNa-B25-4 catalyst requires a pretreatment step to achieve high activity in CO_2 hydrogenation.

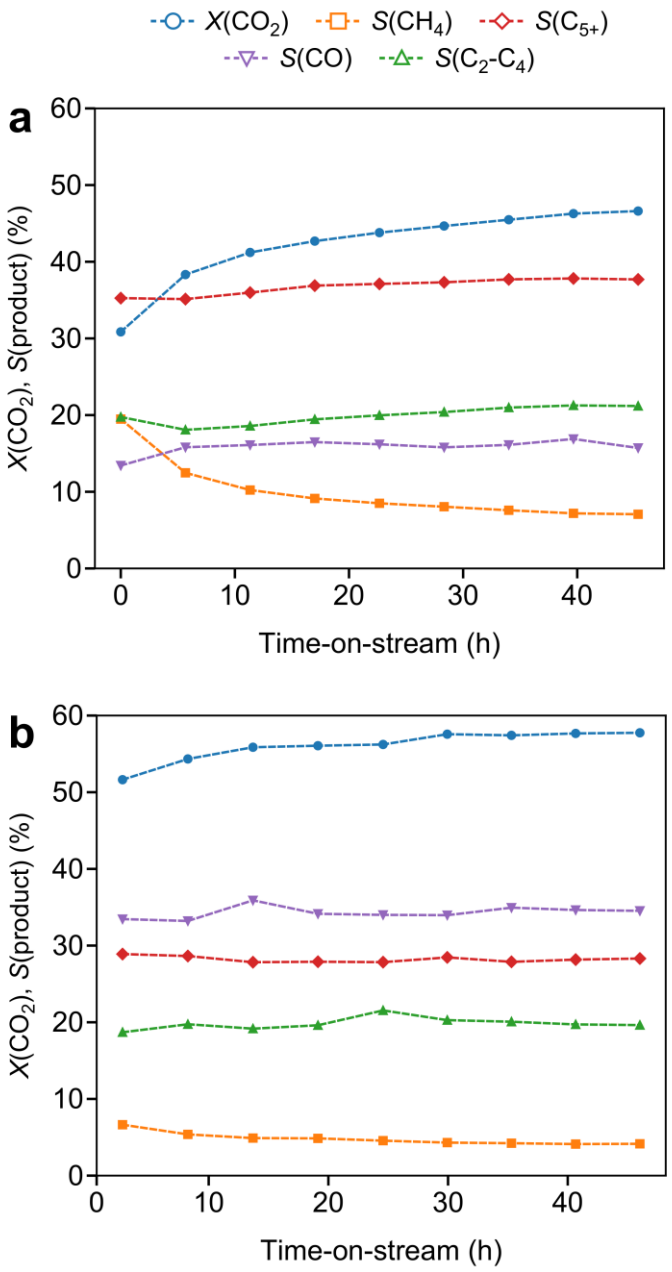


Fig. S2. **Effect of pretreatment on the evolution of catalytic performance of FeCoNa-B25-4 during CO_2 hydrogenation.** (a) CO_2 hydrogenation without prior pretreatment and (b) CO_2 hydrogenation after H_2 reduction at 400 °C for 20 h and H_2/CO activation at 300 °C and 10 bar for 24 h. Reaction conditions: H_2/CO_2 = 3, T = 350 °C, P = 30 bar, and GHSV = 5732 $cm^3\ h^{-1}\ g_{cat}^{-1}$.

To probe the structural origin of this pretreatment-induced enhancement, XRD analysis was performed on FeCoNa-B25-4 after different treatment stages (**Fig. S3**). The fresh catalyst is

dominated by the metallic FeCo phase, with Rietveld analysis showing 88.87 wt.% FeCo and 11.13 wt.% Fe_5C_2. After the reduction and activation treatment, the Fe_5C_2 fraction increases markedly to 44.44 wt.%, while the FeCo fraction decreases to 55.56 wt.%, confirming that the H_2 reduction followed by CO/H_2 activation promotes carburisation of the initially metallic FeCo-rich precursor. This formation of iron carbide helps explain the enhanced C_{5+} selectivity observed after pretreatment, since Fe_5C_2 is commonly associated with Fischer-Tropsch chain-growth activity.

Upon introducing the CO_2 hydrogenation feed for 2 h, the catalyst undergoes further restructuring, with the appearance of Fe_3O_4 together with FeCo and Fe_5C_2 phases. The formation of Fe_3O_4 indicates that CO_2 acts as a soft oxidant under reaction conditions, partially oxidising the reduced/carburised catalyst while preserving a significant carbide fraction. After extended reaction, the spent catalyst contains predominantly Fe_3O_4 and Fe_5C_2. These results show that the initially metallic DJS-derived FeCo-rich catalyst does not remain as the dominant steady-state phase. Instead, reduction-activation first promotes carburisation, followed by partial oxidation and further restructuring under CO_2 hydrogenation, ultimately generating the mixed oxide-carbide ensemble associated with high catalytic performance.

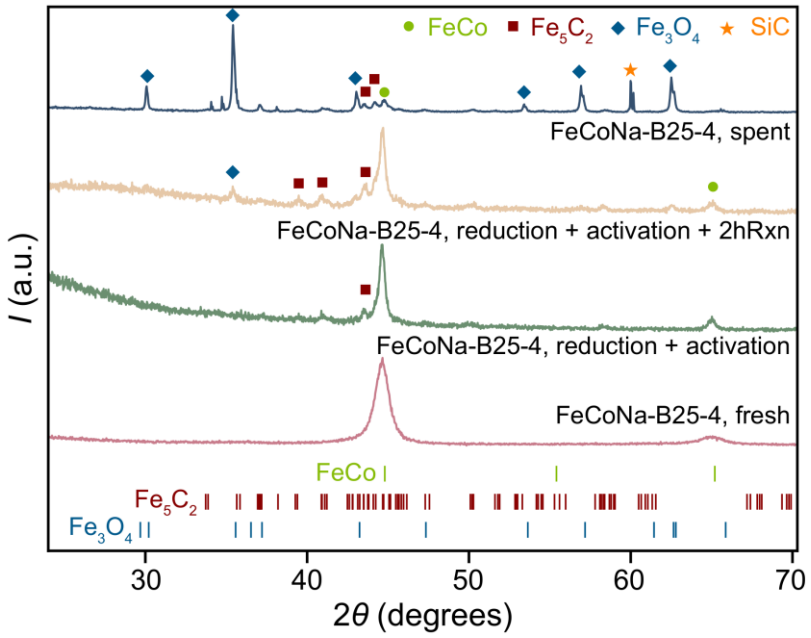


Fig. S3. Structural evolution of FeCoNa-B25-4 during pretreatment and CO_2 hydrogenation. Powder XRD patterns of the fresh, pretreated, 2 h reacted, and spent catalyst, showing carburisation during pretreatment followed by formation of a mixed Fe_3O_4-Fe_5C_2 working state during CO_2 hydrogenation.

Table S2. Catalytic performance of FeCoNa-B25-4 and FeCoNa-B30-4 at different reaction temperatures (30 bar, 5732 $cm^3\ h^{-1}\ g_{cat}^{-1}$ GHSV).

Entry	Catalyst	*T* (°C)	*X*(CO_2) (%)	*S*(CH_4) (%)	*S*(C_{5+}) (%)	*Y*(C_{5+}) (%)
1	FeCoNa-B25-4	350	57.6	19.9	34.5	19.9
2	FeCoNa-B30-4	350	41.1	19.4	47.8	19.6
3	FeCoNa-B25-4	370	58.1	25.5	30.9	18.0
4	FeCoNa-B30-4	370	59.6	26.2	34.1	20.3

Table S3. CO_2 conversion and product selectivity of DJS-derived FeNa and FeCoNa catalysts, during CO_2 hydrogenation at 350 °C, 30 bar, and a GHSV of 5732 $cm^3\ h^{-1}\ g_{cat}^{-1}$ using an H_2/CO_2 ratio of 3:1. C_5-C_{10} and C_8-C_{16} selectivities are subsets of the total C_{5+} selectivity.

Entry	Catalyst	*X*(CO_2) (%)	*S*(CH_4) (%)	*S*(CO) (%)	*S*(C_2-C_4-) (%)	*S*(C_2-C_4=) (%)	*S*(*R*-OH) (%)	*S*(C_{5+}) (%)	*S*(C_5-C_{10}) (%)	*S*(C_8-C_{16}) (%)
1	FeNa-B25-4	52.2	17.1	6.2	5.9	28.3	3.3	39.3	23.1	20.7
2	FeCoNa	35.7	28.9	27.5	14.7	11.3	1.9	15.7	4.9	10.7
3	FeCoNa-B25-2	50.2	19.9	6.9	10.0	28.1	4.6	30.5	20.5	12.1
4	FeCoNa-B25-4	57.6	19.9	4.2	9.8	28.2	3.3	34.5	21.1	15.8
5	FeCoNa-B25-8	59.1	23.2	3.6	10.4	26.2	2.8	33.8	20.8	15.3
6	FeCoNa-B30-4	41.1	19.4	2.4	5.7	21.6	3.0	47.8	25.7	25.0
7	FeCoNa-B25-4-Ar	57.3	19.6	4.1	7.5	23.8	2.9	42.1	23.0	23.9

S2.3 Comparison of catalytic performance and stability with literature catalysts

Comparison with representative literature catalysts (**Table 1**) highlights the strong combination of activity and C_{5+} productivity achieved by the DJS-derived catalysts. DJS-derived FeNa-B25-4 achieves 52.2% CO_2 conversion and a C_{5+} yield of 20.5%, with gasoline- and jet-fuel-range selectivities of 23.1% and 20.7%, respectively (**Table S3**). Incorporating Co and optimising milling under Ar further increases the C_{5+} yield to 24.1% at 57.3% conversion. At 350 °C and

30 bar, doubling the GHSV from 5732 to 11464 $cm^3\ h^{-1}\ g_{cat}^{-1}$ approximately doubles the C_{5+} space-time yield (STY) from 0.20 to 0.40 $g_{C5+}\ h^{-1}\ g_{cat}^{-1}$ while preserving the single-pass C_{5+} yield. This is the highest C_{5+} STY among the catalysts compiled in **Table 1**. FeCoNa-B25-4-Ar also combines high conversion with substantially greater C_{5+} yield than the FeCo catalyst reported by Pan et al.: at nearly identical CO_2 conversion (57.3% versus 57.8%), it achieves 24.1% versus 14.0% C_{5+} yield, at a higher GHSV of 5,732 versus 4,000 $cm^3\ h^{-1}\ g_{cat}^{-1}$.[16] FeCoNa-B25-4-Ar achieves a C_{5+} yield comparable to that of the Co-promoted Fe catalyst reported by Jiang et al. at approximately tenfold higher GHSV (5,732 versus 560 $cm^3\ h^{-1}\ g_{cat}^{-1}$), corresponding to C_{5+} STYs of 0.20 and 0.02 $g_{C5+}\ h^{-1}\ g_{cat}^{-1}$, respectively (**Table 1**).[17] Even at the doubled GHSV, FeCoNa-B25-4-Ar retains 52.1% CO_2 conversion and 23.7% C_{5+} yield; its C_{5+} STY of 0.40 $g_{C5+}\ h^{-1}\ g_{cat}^{-1}$ exceeds the values listed for Na-Zn-Fe (0.29) and KZFe-5.0Co (0.23).[18,19] KZFe-5.0Co achieves a higher single-pass C_{5+} yield of 26.7%, but FeCoNa-B25-4-Ar combines its higher productivity with a 500 h stability assessment, compared with 60 h for KZFe-5.0Co.

Long-term stability further distinguishes FeCoNa-B25-4-Ar from reported Fe-based CO_2 hydrogenation catalysts. A revealing comparison is CoFe-0.81Na: during its 120 h test, conversion fell from 14.8% to 10.6% in the first 28 h, a relative decrease of approximately 28%, while CO selectivity did not stabilise until approximately 110-120 h.[20] Its spent-catalyst XRD and Co/Fe-edge spectroscopy were obtained after 48 h, rather than at the end of the stability test. For Liang *et al.*'s 1Na/Fe catalyst, CO_2 conversion fell from approximately 53% at 1 h to 40% by 3 h and 37% by 10 h.[21] Other catalysts demonstrate stability over shorter periods: ex-$CuFeO_2$ maintained conversion and C_{5+} selectivity for 100 h, at approximately 17% CO_2 conversion;[22] and KZFe-5.0Co maintained high activity and C_{5+} selectivity for 60 h, achieving 50.2% conversion and 26.7% C_{5+} yield, although its spent-catalyst XRD was obtained after only 8 h.[19] For FeNa(1.18), CO_2

conversion decreased from approximately 44% to 40% during the first 20-30 h, whereas its light-olefin selectivity remained approximately constant.[23] Na-CoCu/TiO_2 was evaluated for 200 h, maintaining only 18% conversion and 40% C_{5+} selectivity under different reaction conditions.[24] Albrecht *et al.* also demonstrated substantial durability for Fe_2O_3-CT600; although temperature and feed composition were varied during their 280 h experiment, repeating the initial conditions near its end showed that CO_2 conversion was largely retained.[25] The distinguishing result is therefore the retention of substantial CO_2 conversion and C_{5+} selectivity over 500 h under fixed conditions, with Fe_5C_2 and FeCo identified in the catalyst recovered at the end of that test.

S3. N_2-sorption

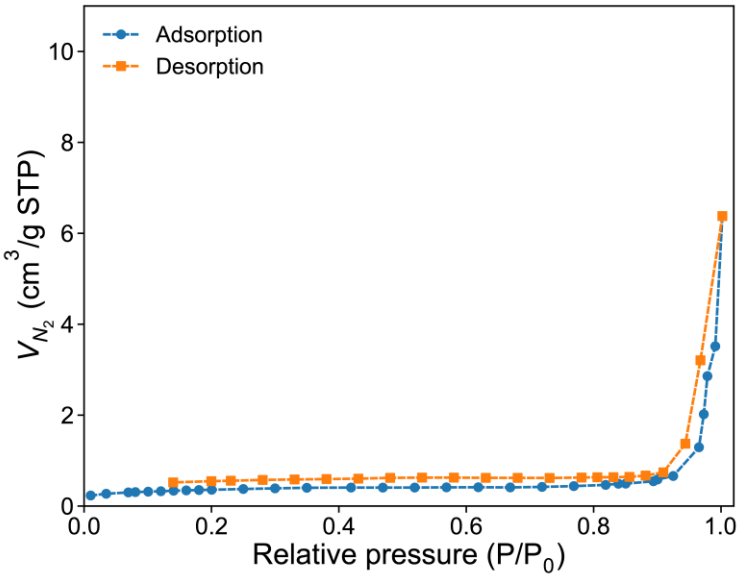


Fig. S4. Textural properties of the FeCoNa catalyst. N_2 adsorption-desorption isotherm of FeCoNa before mechanochemical treatment, showing low N_2 uptake consistent with its low BET surface area and pore volume.

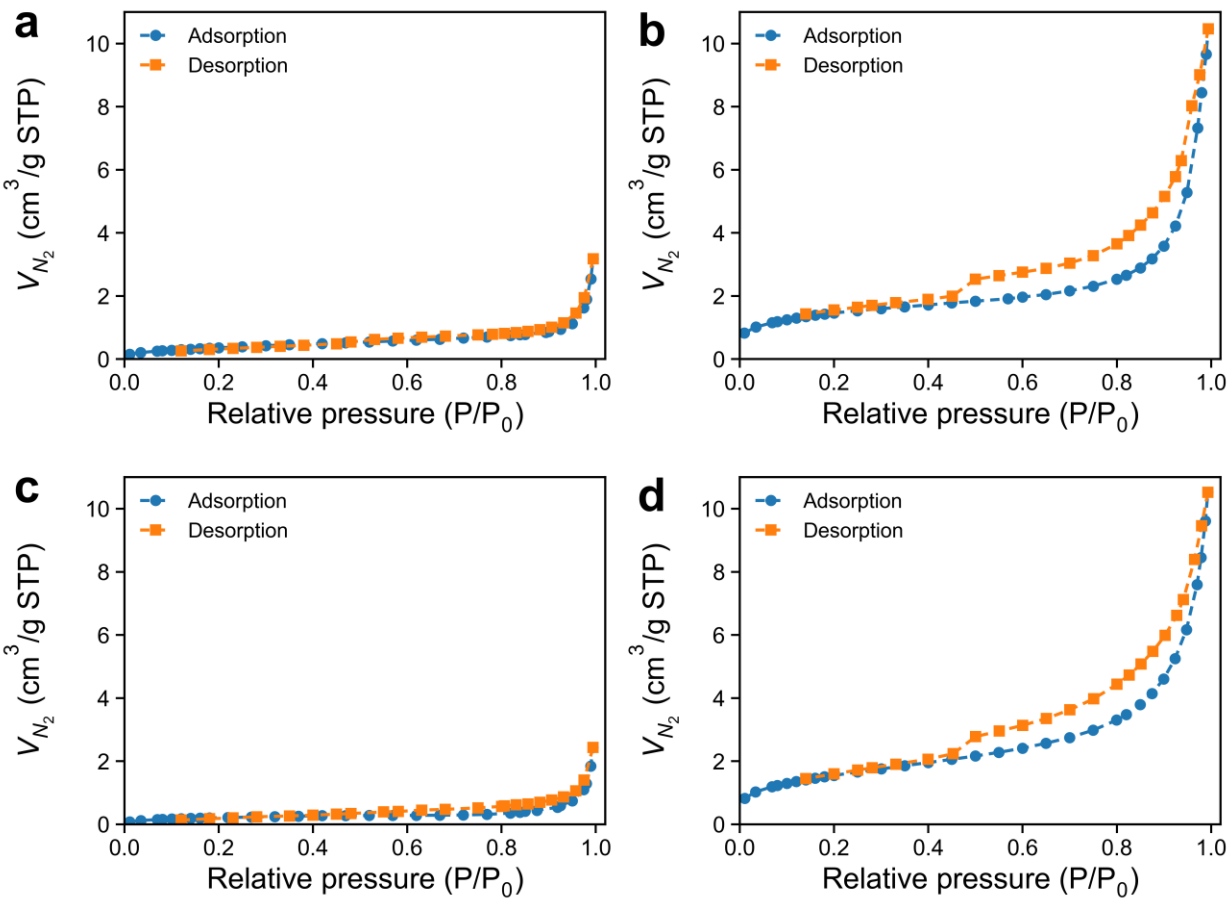


Fig. S5. Evolution of textural properties of DJS-derived catalysts. N_2 adsorption-desorption isotherms of fresh and spent **(a,b)** FeCoNa-B25-4, and **(c,d)** FeCoNa-B25-4-Ar, showing an increase in surface area for the DJS-derived catalysts after CO_2 hydrogenation.

S4. SEM, XPS and surface characterisation

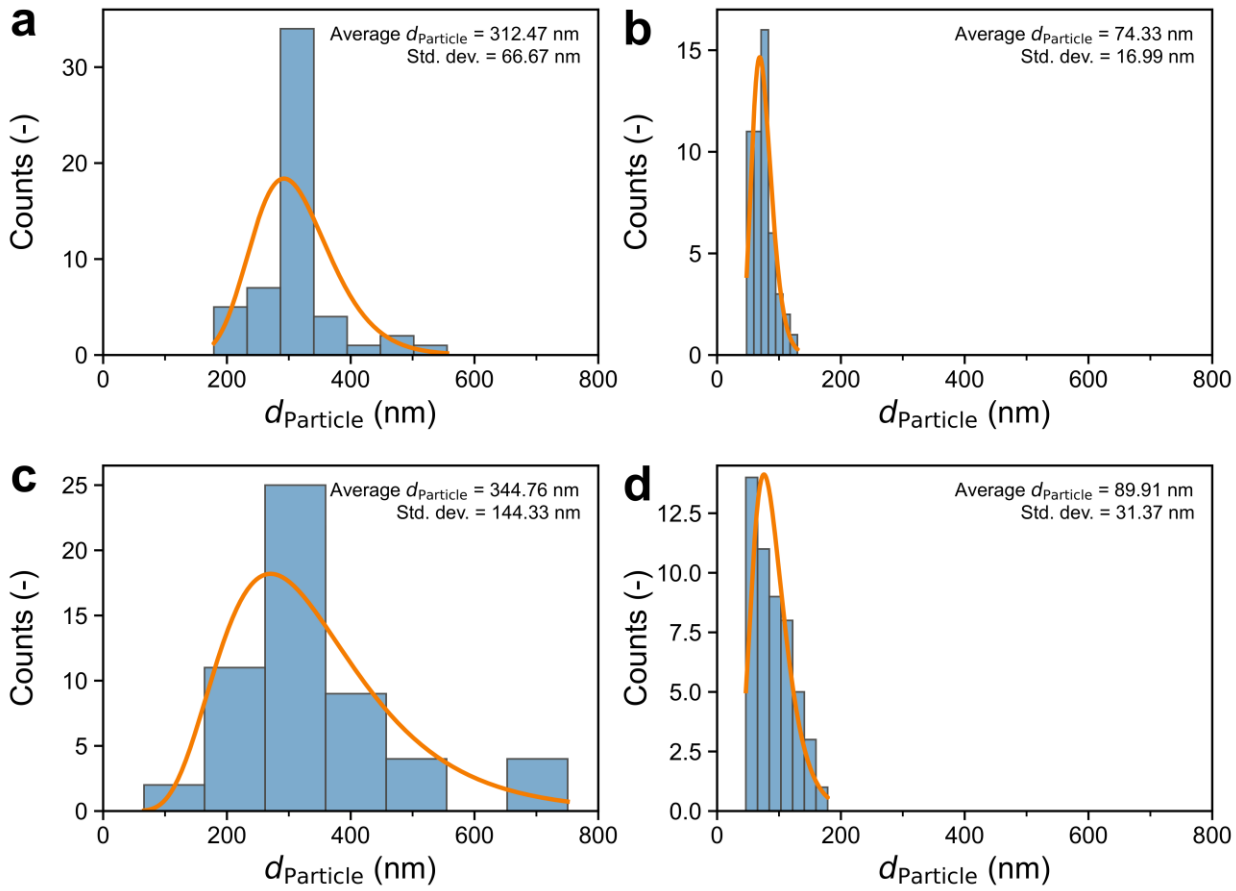


Fig. S6. **Particle-size evolution of DJS-derived catalysts during CO_2 hydrogenation.** HR-TEM-derived particle-size distributions of (a) fresh FeCoNa-B25-4, (b) spent FeCoNa-B25-4, (c) fresh FeCoNa-B25-4-Ar, and (d) spent FeCoNa-B25-4-Ar, determined from Transmission electron microscopy image analysis.

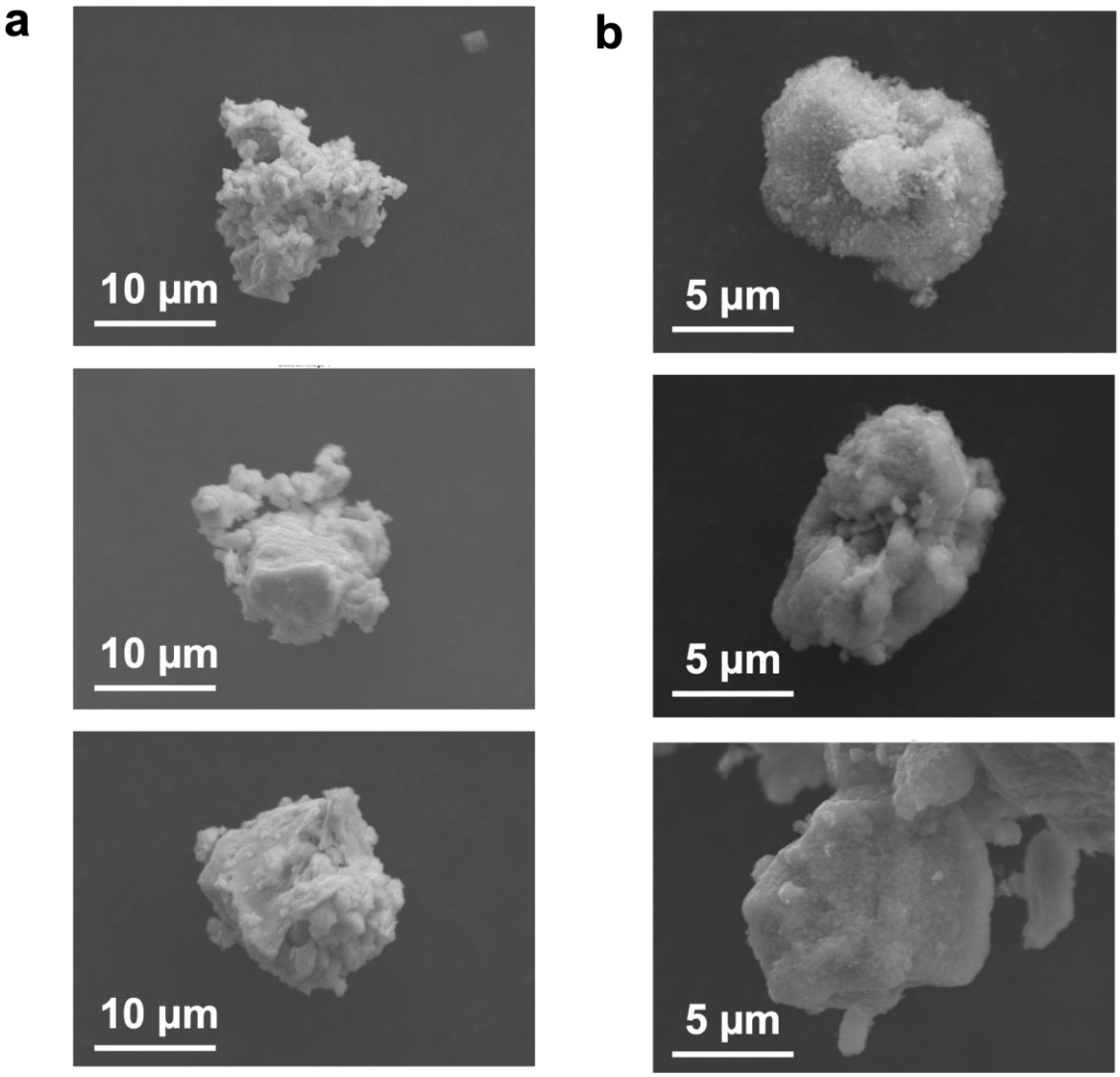


Fig. S7. **Morphological evolution of FeCoNa-B25-4-Ar during CO_2 hydrogenation.** SEM analysis of (a) fresh FeCoNa-B25-4-Ar and (b) spent FeCoNa-B25-4-Ar catalysts.

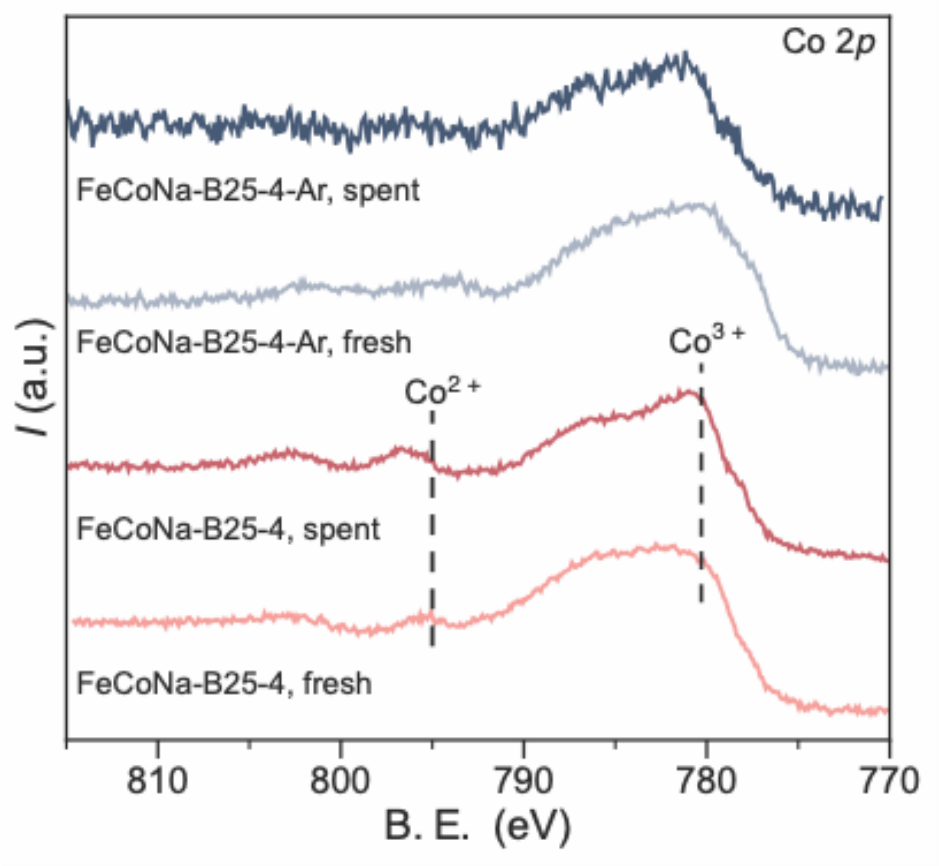


Fig. S8. **Evolution of Co surface oxidation states in fresh and spent FeCoNa catalysts.** Co 2*p* XPS spectra of fresh and spent DJS-derived catalysts.

S5. Long-term stability and thermal behaviour of DJS-made FeCoNa catalyst during CO_2 hydrogenation

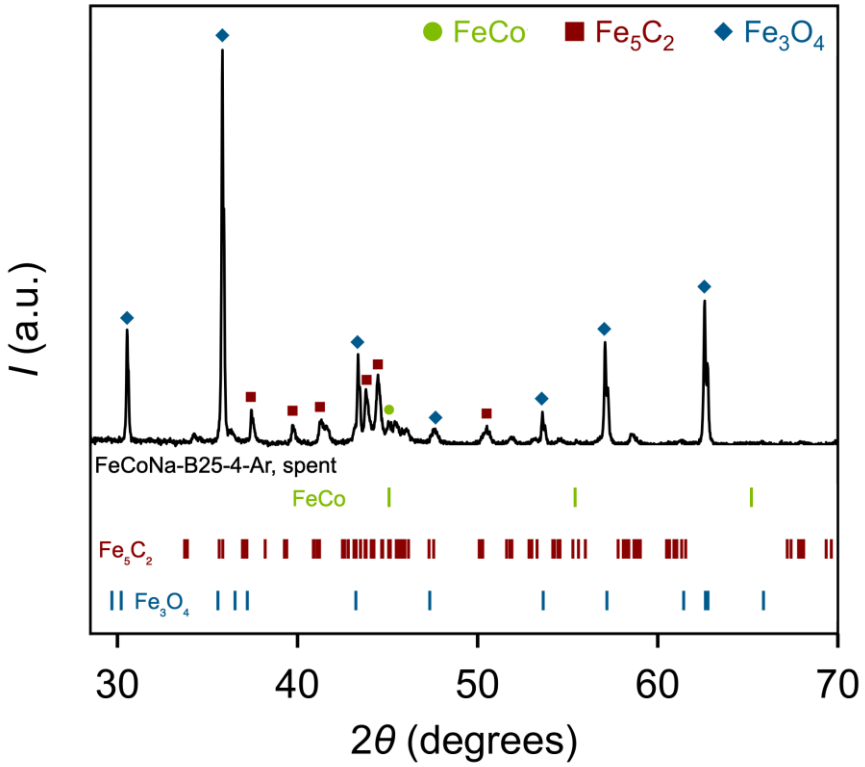


Fig. S9. **Phase stability of DJS-derived catalyst after long-term CO_2 hydrogenation.** Powder X-ray diffraction patterns of the spent FeCoNa-B25-4-Ar catalyst recovered after 500 h of continuous CO_2 hydrogenation, showing the retained mixed Fe_3O_4-Fe_5C_2-FeCo phase assemblage.

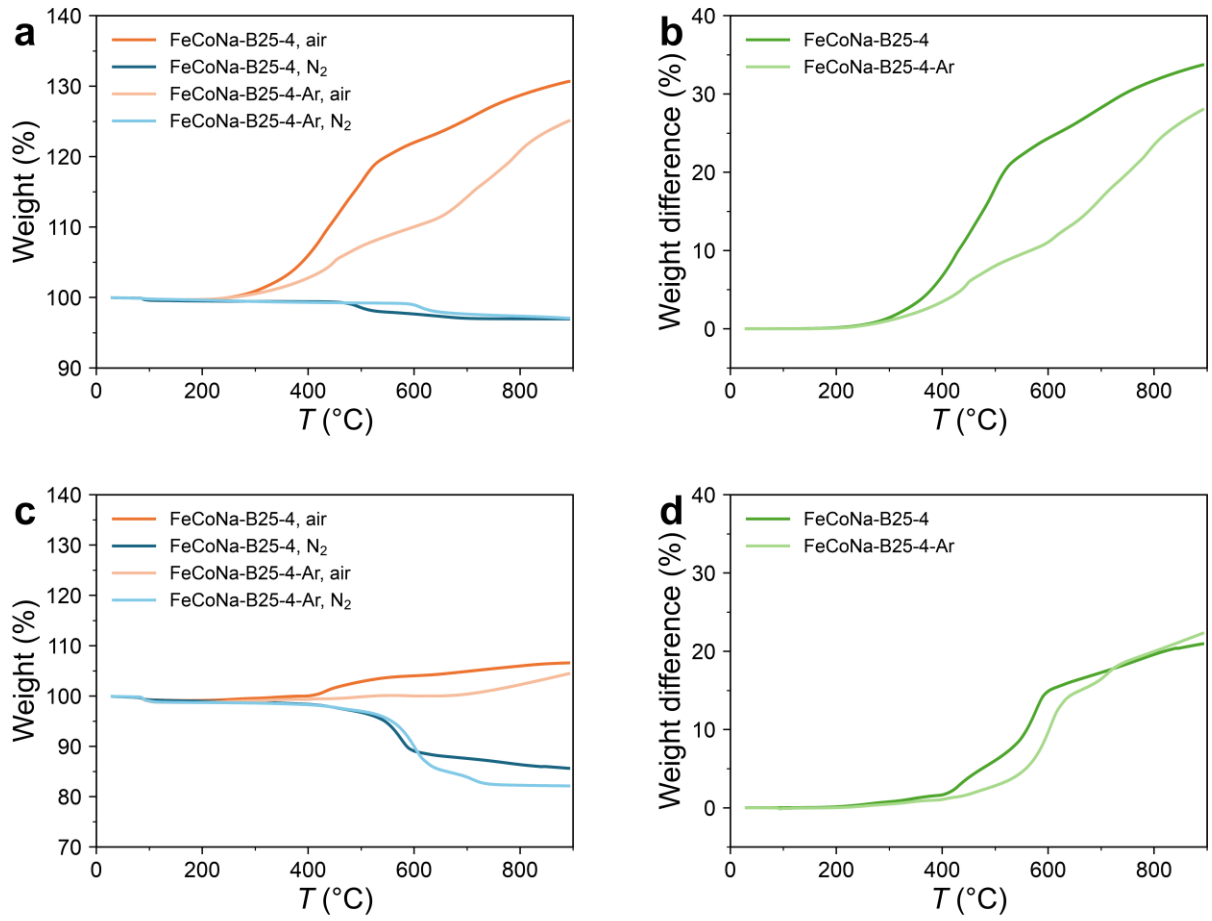
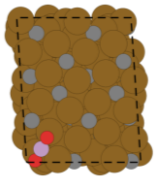
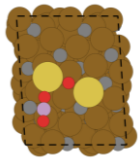
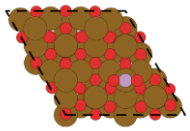
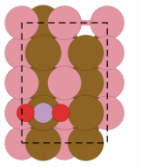
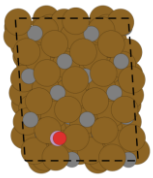
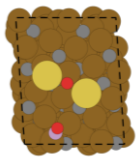
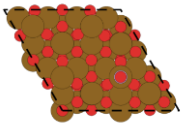
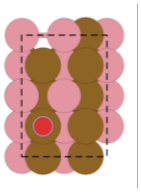
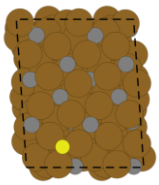
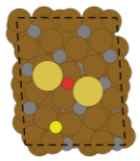
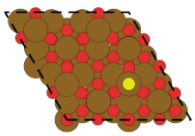
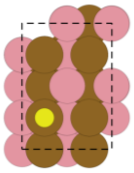
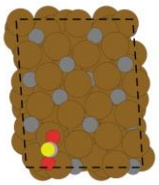
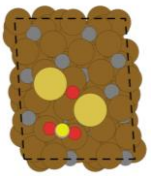
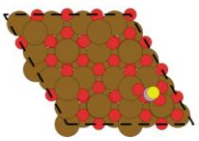
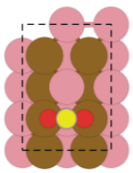
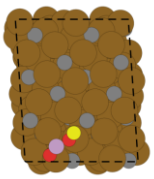
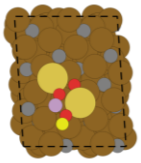
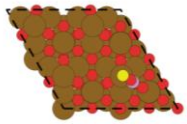
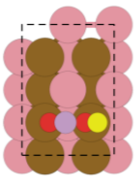
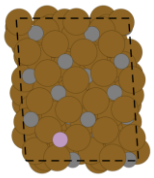
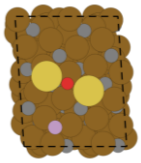
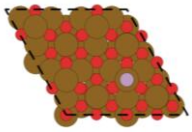
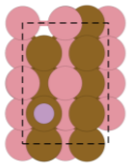
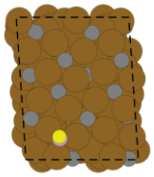
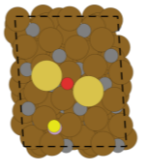
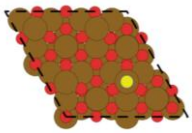
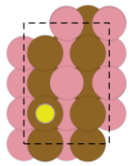
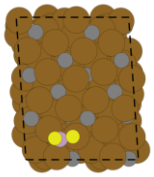
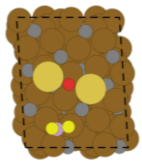
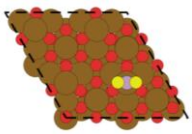
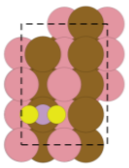
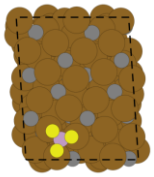
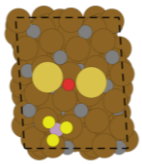
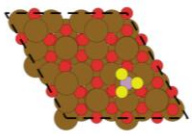
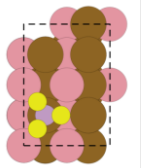
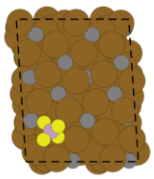
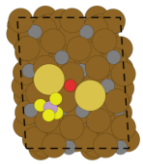
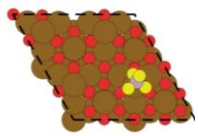
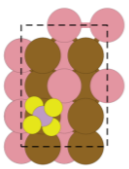


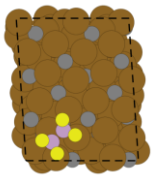
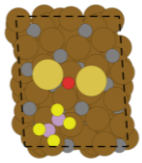
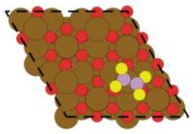
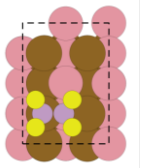
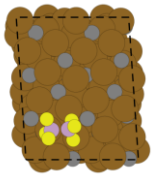
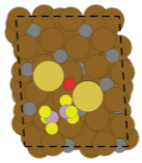
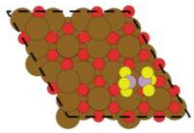
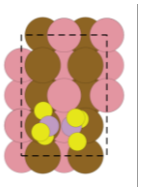
Fig. S10. **Thermogravimetric analysis of FeCoNa-B25-4 and FeCoNa-B25-4-Ar.** (a) Weight profiles of the fresh catalysts measured separately under air and N_2. (b) Corresponding weight differences (air - N_2) for the fresh catalysts. (c) Weight profiles of the catalysts recovered after 24 h of CO_2 hydrogenation, measured separately under air and N_2. (d) Corresponding weight differences (air - N_2) for the spent catalysts. Samples were heated from room temperature to 900 °C at 10 °C min^{-1}, with a gas flow rate of 20 mL min^{-1}. The change in sample weight below 400 °C is associated with the loss or burning of surface carbonaceous deposits, and that above 400 °C is associated with phase changes of metallic and/or carbidic Fe, specifically sequential oxidation to more oxidised forms when measured under air.[26] Due to the higher molar mass of oxides compared to the corresponding carbide or metal, a sharp increase in percentage weight difference between A and B can be used as a proxy indicator for phase oxidation.

S6. Computational analysis

Table S4. Top view of all adsorbates on the four catalyst surfaces: Fe_5C_2(510), Fe_5C_2(510) + Na_2O, Fe_3O_4(111), and FeCo(110). Dashed lines denote the surface unit cell. Atoms are coloured by element: Fe (brown), C of the carbide (grey), O (red), Na (dark yellow), Co (pink), and H (yellow) atoms, and C of the adsorbate (purple).

Adsorbent	Fe_5C_2(510)	Fe_5C_2(510) + Na_2O	Fe_3O_4(111)	FeCo(110)
CO_2				
CO				
H				
HCOO				
COOH				

C				
CH				
CH_2				
CH_3				
CH_4				

C_2H_4				
C_2H_6				

S7. Supplementary references

1. Pham, T. H., Duan, X., Qian, G., Zhou, X. & Chen, D. CO Activation Pathways of Fischer–Tropsch Synthesis on χ-Fe_5C_2 (510): Direct versus Hydrogen-Assisted CO Dissociation. *J. Phys. Chem. C* **118**, 10170–10176 (2014).
2. Hofer, L. J. E. & Cohn, E. M. Saturation Magnetizations of Iron Carbides. *J. Am. Chem. Soc.* **81**, 1576–1582 (1959).
3. Retief, J. J. Powder diffraction data and Rietveld refinement of Hägg-carbide, χ-Fe_5C_2. *Powder Diffr.* **14**, 130–132 (1999).
4. Sorescu, D. C. Plane-Wave Density Functional Theory Investigations of the Adsorption and Activation of CO on Fe_5C_2 Surfaces. *J. Phys. Chem. C* **113**, 9256–9274 (2009).
5. Zhao, S. *et al.* Surface morphology of Hägg iron carbide (χ-Fe_5C_2) from *ab initio* atomistic thermodynamics. *J. Catal.* **294**, 47–53 (2012).

6. Yang, T. *et al.* Structure and energetics of hydrogen adsorption on Fe_3O_4(111). *J. Mol. Catal. A: Chem.* **302**, 129–136 (2009).
7. Su, T. *et al.* Density functional theory study on the interaction of CO_2 with Fe_3O_4(111) surface. *Appl. Surf. Sci.* **378**, 270–276 (2016).
8. Horton, M. K., Montoya, J. H., Liu, M. & Persson, K. A. High-throughput prediction of the ground-state collinear magnetic order of inorganic materials using Density Functional Theory. *npj Comput. Mater.* **5**, 64 (2019).
9. Moore, G. C. *et al.* High-throughput determination of Hubbard U and Hund J values for transition metal oxides via the linear response formalism. *Phys. Rev. Mater.* **8**, 014409 (2024).
10. Mizuno, M., Araki, H. & Shirai, Y. First Principles Calculation of Defect and Magnetic Structures in FeCo. *Mater. Trans.* **47**, 2646–2650 (2006).
11. Gholizadeh, H. & Hasani, S. *Ab-initio* calculation of the γ-surface and cleavage energy in the B2 FeCo intermetallic compound. *Comput. Mater. Sci.* **143**, 515–527 (2018).
12. Fu, C. L. & Krčmar, M. First-principles study of the structural, defect, and mechanical properties of B2 FeCo alloys. *Phys. Rev. B* **74**, 174108 (2006).
13. Aho, A. *et al.* Effect of Cu-Fe-Co Catalyst Pretreatment in Higher Alcohol Synthesis. *Top. Catal.* https://doi.org/10.1007/s11244-026-02289-y (2026).
14. Stanke, A. *et al.* Cobalt-promoted Fe_3O_4 catalysts for CO_2 hydrogenation to C_{2+} hydrocarbons: Effect of pretreatment method and reaction temperature. *Fuel Process. Technol.* **288**, 108467 (2026).
15. Yao, B. *et al.* Transforming carbon dioxide into jet fuel using an organic combustion-synthesized Fe-Mn-K catalyst. *Nat. Commun.* **11**, 6395 (2020).

16. Pan, M. *et al.* Unraveling the role of reaction intermediates in CO_2 hydrogenation to light aromatics over iron-based multifunctional catalysts. *Appl. Catal. B: Environ. Energy* **398**, 127033 (2026).
17. Jiang, F., Liu, B., Geng, S., Xu, Y. & Liu, X. Hydrogenation of CO_2 into hydrocarbons: enhanced catalytic activity over Fe-based Fischer–Tropsch catalysts. *Catal. Sci. Technol.* **8**, 4097–4107 (2018).
18. Zhang, Z. *et al.* Zn and Na promoted Fe catalysts for sustainable production of high-valued olefins by CO_2 hydrogenation. *Fuel* **309**, 122105 (2022).
19. Guo, L. *et al.* High-yield production of liquid fuels in CO_2 hydrogenation on a zeolite-free Fe-based catalyst. *Chem. Sci.* **14**, 171–178 (2023).
20. Zhang, L. *et al.* Direct conversion of CO_2 to a jet fuel over CoFe alloy catalysts. *The Innovation* **2**, 100170 (2021).
21. Liang, B. *et al.* Effect of Na Promoter on Fe-Based Catalyst for CO_2 Hydrogenation to Alkenes. *ACS Sustain. Chem. Eng.* **7**, 925–932 (2019).
22. Choi, Y. H. *et al.* Carbon dioxide Fischer-Tropsch synthesis: A new path to carbon-neutral fuels. *Appl. Catal. B: Environ.* **202**, 605–610 (2017).
23. Wei, J. *et al.* New insights into the effect of sodium on Fe_3O_4-based nanocatalysts for CO_2 hydrogenation to light olefins. *Catal. Sci. Technol.* **6**, 4786–4793 (2016).
24. Shi, Z. *et al.* Effect of alkali metals on the performance of $CoCu/TiO_2$ catalysts for CO_2 hydrogenation to long-chain hydrocarbons. *Chin. J. Catal.* **39**, 1294–1302 (2018).
25. Albrecht, M. *et al.* Unexpectedly efficient CO_2 hydrogenation to higher hydrocarbons over non-doped Fe_2O_3. *Appl. Catal. B Environ.* **204**, 119–126 (2017).

26. Wu, W. *et al.* Facet sensitivity of iron carbides in Fischer-Tropsch synthesis. *Nat. Commun.* **15**, 6108 (2024).